$\pi-\sigma$ Decomposition of the Electronic Activity in Competing [5,6] and [6,6] Cycloaddition Reactions Between C$_{60}$ and Cyclopentadiene

Nery Villegas-Escobar[†,♯], Albert Poater[‡], Miquel Solà[‡], Henry F. Schaefer III[♯,*] and Alejandro Toro-Labbé[†,*]

[†]*Laboratorio de Química Teórica Computacional (QTC), Facultad de Química, Pontificia Universidad Católica de Chile, Avenida Vicuña Mackenna 4860, Santiago, Chile.*

[‡] *Institut de Química Computacional i Catàlisi (IQCC) and Departament de Química, Universitat de Girona, Mª Aurèlia Capmany 69, 17003 Girona, Catalonia, Spain.*

[♯] *Center for Computational Quantum Chemistry, University of Georgia, Athens, Georgia 30602 USA.*

Email: ccq@uga.edu ; atola@puc.cl

Abstract

In this work, a comprehensive study of the electronic activity that takes place in the cycloaddition between C_{60} and cyclopentadiene toward the $[5,6]$ and $[6,6]$ reaction pathways is presented. These are competitive reaction mechanisms dominated by σ and π fluctuating activity. To better understand the electronic activity at each stage of the mechanism, the reaction force (RF) and the symmetry-adapted reaction electronic flux (SA-REF, $J_{\Gamma_i}(\xi)$) have been used helping to elucidate whether π or σ bonding changes drive the reaction. Since the studied cycloaddition reaction proceed through a C_S symmetry reaction path, two SA-REF are constructed: $J_{A'}(\xi)$ and $J_{A''}(\xi)$. In particular, $J_{A'}(\xi)$ accounts for bond transformation associated with π bonds, while $J_{A''}(\xi)$ is sensitive toward σ bonding changes. It was found that the $[6,6]$ path is highly favored over the $[5,6]$ regarding activation energies. This difference is primarily due to the less intensive electronic reordering of the σ electrons in the $[6,6]$ path, as a result of the pyramidalization of carbon atoms in C_{60} ($sp^2 \longrightarrow sp^3$ transition). Interestingly, no substantial differences in the π electronic activity from the reactant complex to the transition state structure were found when comparing the $[5,6]$ and $[6,6]$ paths. Partition of the kinetic energy into its symmetry contributions indicates that when a bond is being weakened/broken (formed/strengthened) non-spontaneous (spontaneous) changes in the electronic activity occur, thus prompting an increase (decrease) of the kinetic energy. Therefore, contraction (expansion) of the electronic density in the vicinity of the bonding change is expected to take place.

Bond formation: $\downarrow T \Rightarrow \downarrow \mu \Rightarrow \uparrow \rho(\mathbf{r}) \Rightarrow \uparrow J(\xi)$

Bond Breaking: $\uparrow T \Rightarrow \uparrow \mu \Rightarrow \downarrow \rho(\mathbf{r}) \Rightarrow \downarrow J(\xi)$

1 Introduction

Fullerenes with a number of potential applications in many fields that range from material science to medicinal chemistry are important molecular entities in nanochemistry [1–3]. The most prominent representative of the fullerene family is C_{60}. This molecule behaves as a poly-olefin poor in electrons (with strong electron-withdrawing character). As a result, it undergoes a variety of chemical organic reactions, the most important being the nucleophilic additions [4–6]. Moreover, C_{60} reacts through many metal-catalysed processes like the Pauson-Khand reactions [7–9], the Suzuki-Miyaura reactions [10–13] or the $[2 + 2 + 2]$ cycloadditions [14–16], among others. However, one of the most employed reactions for the functionalization of fullerenes and their derivatives is the Diels-Alder (DA) cycloaddition [17–22]. The electron-withdrawing nature of C_{60} makes this molecule an ideal dienophile for DA reactions [23]. The functionalization of C_{60} through the DA reaction can yield many different products as a result of monoaddition, bisaddition and so on up to six consecutive additions [24, 25]. In some cases, adducts formed are thermally unstable and can undergo cycloreversion [26].

C_{60} has two different types of C-C bonds (see Figure 1). Corannulenic $[5, 6]$ bonds are located between an hexagon and a pentagon, whereas the pyracylene $[6, 6]$ bonds are found in the hexagon-hexagon ring junctions [27]. The Diels-Alder reaction in empty fullerenes show an almost exclusive preference for the $[6, 6]$ versus the $[5, 6]$ bonds [5, 6, 28, 29]. The $[5, 6]$ becomes favored or at least competitive in some endohedral metallofullerenes (EMFs) [30]. For chemists working in the reactivity of fullerenes, it would be fascinating to have a full control on the regioselectivity of the DA reactions. Interestingly, the $[5, 6]$ attack was computationally found to be favored in strongly reduced C_{60} cages [31] and in high spin states [32]. The accumulation of negative charge or spin density takes place in the 5-membered rings (5-MRs) of C_{60}. Consequently, the aromaticity of the 5-MRs increases and the $[5, 6]$ attack becomes preferred because it breaks the aromaticity of only an aromatic 5-MR [33], whereas the $[6, 6]$ attack destroys the aromaticity of two aromatic 5-MRs.

In general, functionalization of fullerenes and EMFs occurs regioselectivity in a unique or

few addition sites [34]. It would be desirable to have a full control on the regioselectivity of additions to fullerenes and EMFs in such a way that chemists could fully determine the addition pattern in a given functionalization process. To move forward to this objective, it is necessary to have a deep understanding of the reasons of the high regioselectivity of fullerenes toward $[6,6]$ bonds. The main aim of the present work is to provide insight into the question of why the DA cycloaddition to C_{60} occurs exclusively at the $[6,6]$ bonds using computational tools derived from the conceptual Density Functional Theory (CDFT).
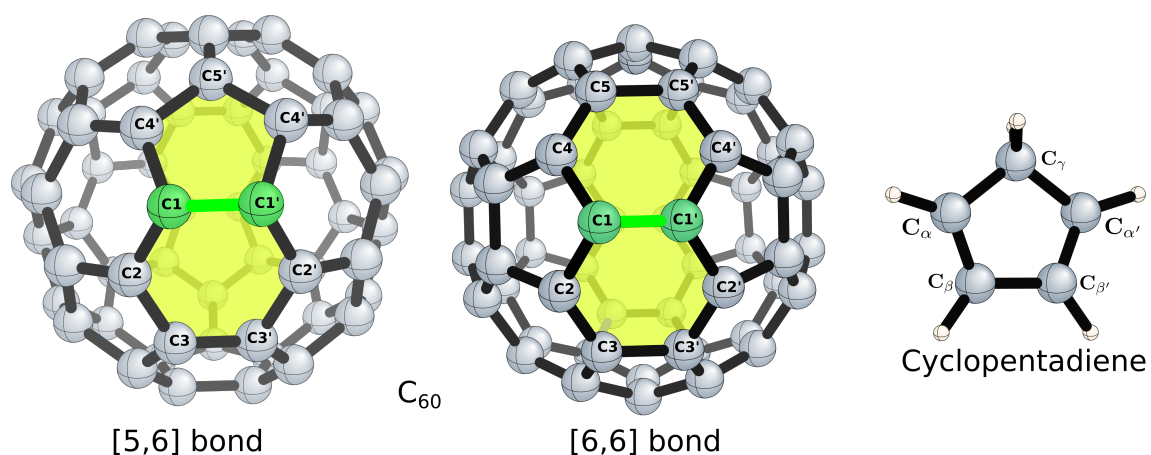
Figure 1: Two types of bond in fullerene (C_{60}) schematized along with cyclopentadiene. Labeling of the relevant atoms is shown.

2 Theory

2.1 Reaction Force

The reaction force (RF) is obtained as the derivative of the energy with respect to the reaction coordinate (ξ) [35, 36]:

$$F(\xi) = -\frac{dE(\xi)}{d\xi} \tag{1}$$

Computation of $F(\xi)$ is possible by obtaining an energy profile through the intrinsic reaction coordinate procedure (IRC$\equiv \xi$) [37–39], which allows one to obtain the minimum energy path for the transformation of reactants into products passing by a transition state. The RF formalism allows the partitioning of the reaction coordinate into different regions where different reaction events might be taking place [40–42]. The boundaries of reaction regions are obtained from the critical points on the $F(\xi)$ profile, a minimum at ξ_1 before the transition state and a maximum at ξ_2 thereafter [43]. Figure 2 displays a generic energy (**a**) and reaction force (**b**) profiles along with the partition of the reaction coordinate. For a reaction with a single transition state, three reaction regions are defined: reactant region **RR** ($\xi_R \leq \xi < \xi_1$), transition state region **TSR** ($\xi_1 \leq \xi \leq \xi_2$) and product region **PR** ($\xi_2 < \xi \leq \xi_P$) [42, 44]. For reactions taking place via more than one elementary step, more reaction regions have to be considered [45].

In the **RR** structural reordering we emphasize structural deformations and geometrical changes that prepare reactants leading to the formation of activated reactants at ξ_1. The **TSR** is particularly dominated by electronic reordering; within this region most bonding changes take place. In this region a number of transient structures coalesces, where too vague states gather and intensive electronic activity stressing bond breaking and formation processes takes place [46, 47]. After the **TSR**, structural relaxations take over, and the reaction force decreases until reaching the zero value at the product's position, ξ_P. Therefore, the **PR** is characterized by structural relaxations that lead to the final reaction products. It is worth mentioning that the sign and slope of the RF allows one to rationalize the driving forces of a chemical reaction [44, 48]. In addition, the reaction work (W_i) can be defined within each reaction region through numerical integration of the reaction force [42, 48, 49]:

$$W_1 = -\int_{\xi_R}^{\xi_1} F(\xi)\, d\xi > 0 \qquad W_2 = -\int_{\xi_1}^{\xi_{TS}} F(\xi)\, d\xi > 0 \tag{2}$$

$$W_3 = -\int_{\xi_{TS}}^{\xi_2} F(\xi)\, d\xi < 0 \qquad W_4 = -\int_{\xi_2}^{\xi_P} F(\xi)\, d\xi < 0. \tag{3}$$

Since W_1 and W_4 are defined in the **RR** and **PR**, respectively, they primarily account for structural rearrangements, whereas W_2 and W_3, defined within the **TSR**, measure energetics due to electronic reordering [41, 43, 49]. In this context, a phenomenological decomposition of the activation and reaction energies emerges [41, 49]

$$\Delta E^{\ddagger} = \int_{\xi_R}^{\xi_{TS}} F(\xi) d\xi = W_1 + W_2, \tag{4}$$

$$\Delta E^{\circ} = \int_{\xi_R}^{\xi_P} F(\xi) d\xi = W_1 + W_2 + W_3 + W_4. \tag{5}$$
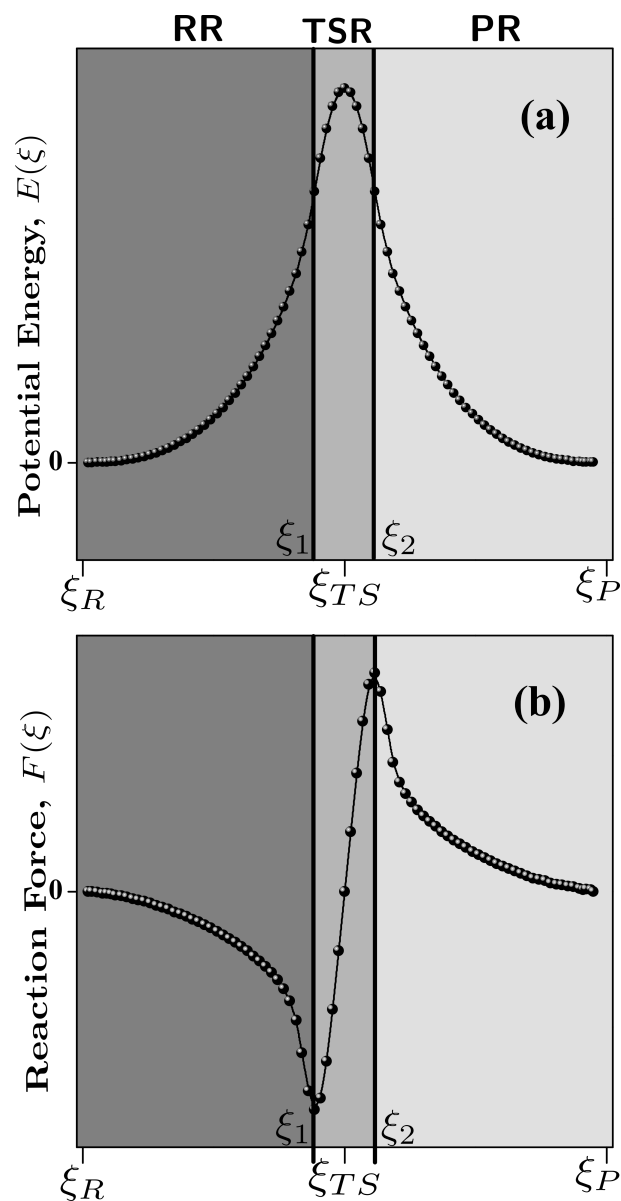
Figure 2: Generic energy (a) and reaction force (b) profiles. Reaction regions are characterized in grey scale. ξ_R, ξ_1, ξ_{TS}, ξ_2 and ξ_P stand for the positions of reactant, activated reactant (force minimum), transition state, activated product (force maximum) and product.

2.2 Symmetry Adapted Reaction Electronic Flux

The reaction electronic flux (REF) has been introduced with the aim of understanding the electronic activity that takes place along a reaction coordinate [50, 51]. It is based on the changes of the electronic chemical potential (CP, μ) in a chemical reaction and defined as:

$$J(\xi) = -\frac{d\mu(\xi)}{d\xi} = -\left(\frac{d\left(\frac{\partial E(\xi)}{\partial N}\right)_{v(\mathbf{r})}}{d\xi}\right) \approx \underbrace{-\frac{1}{2}\left(-\frac{dIP(\xi)}{d\xi} - \frac{dEA(\xi)}{d\xi}\right)}_{\text{FDA}} \approx \underbrace{-\frac{1}{2}\left(\frac{d\epsilon_H(\xi)}{d\xi} + \frac{d\epsilon_L(\xi)}{d\xi}\right)}_{\text{KJT}}$$

$$(6)$$

In density functional theory (DFT) [52], the CP is obtained after differentiation of the energy with respect to N, the total number of electrons of the system, at constant external potential $v(\mathbf{r})$ [52–55]. Since the energy is not a continuous function of N, differentiation is performed by using the finite difference approximation (FDA) [52] that allows one to obtain numerical values of μ in terms of the first ionization potential (IP) and the electron affinity (EA), Eq (6). In analogy with the RF scheme, the $-\frac{dIP(\xi)}{d\xi}$ and $-\frac{dEA(\xi)}{d\xi}$ terms in Eq (6) can be thought as the cation and anion forces, respectively. A further approximation based on the Koopmans' and Janak's theorems (KJT) [56], links IP and EA with the energy of frontier molecular orbitals, HOMO (ϵ_H) and LUMO (ϵ_L) [52, 53, 55], via the last expression in Eq (6).

Regarding the REF, when it is zero no electronic activity beside that of the equilibrium state is deduced. Positive values of the REF indicate spontaneous changes in the electronic density that are driven by bond forming or bond strengthening processes. On the other hand, negative values of $J(\xi)$ are evidence of non-spontaneous electronic activity that is driven by bond weakening or breaking processes [42, 45, 48, 50, 51, 57–60].

For reactions in which symmetry is conserved, degeneracies in the orbital energies may appear, causing nondifferentiable points along the μ profile [61, 62]. To overcome the problem of computing μ, a symmetry adapted extension of the REF has been introduced [61, 62]. For reactions in which a given punctual group ($\mathcal{G}$) is conserved along the reaction path, a symmetry-adapted extension of the CP has been introduced (SA-CP). The SA-CP is obtained in such

a way that to every irreducible representation $\Gamma_s \in \mathcal{G}$ there corresponds a SA-CP, which is computed as shown in Eq. (7) (the reader is referred to ref [61] for derivation of the equations):

$$\mu_s = \frac{1}{2n}(\epsilon_s^{occ} + \epsilon_s^{virt}) \tag{7}$$

where ϵ_s^{occ} and ϵ_s^{virt} stand for the highest occupied and lowest unoccupied molecular orbital energies of symmetry s, respectively; n is the number of irreducible representations of $\mathcal{G}$. The total CP $\mu(\xi)$ is obtained as the sum of the symmetrized CP values:

$$\mu(\xi) = \sum_s^{s \in \mathcal{G}} \mu_s(\xi) \tag{8}$$

Once the SA-CPs are obtained, the SA-REFs are computed by evaluating the negative derivative with respect to the reaction coordinate,

$$J(\xi) = -\left(\frac{d\mu(\xi)}{d\xi}\right) = -\sum_s^{s \in \mathcal{G}} \left(\frac{d\mu_s(\xi)}{d\xi}\right) = \sum_s^{s \in \mathcal{G}} J_s(\xi) \tag{9}$$

According to Eq. (9) the total REF is composed as a sum of individual REF with a given irreducible representation. SA-REF has been succesfully applied to a classical proton transfer in methanethionic O-acid (HO(C=S)H) and two parent Diels Alder reactions: the cycloadditions between butadiene and between ethylene and diacetylene and acetylene, where it was possible to track the electronic activity and distinguish whether π or σ electronic flux is driving the reaction along ξ [61, 62].

3 Computational Details

The cycloaddition reaction between C_{60} and cyclopentadiene was studied with a well-tested DFT method. The M06-2X exchange-correlation functional was used for all atoms. The 6-31g(d) basis set was used together with Truhlar's selected exchange correlation functional. The Berny Synchronous Transit-Guided Quasi-Newton (STQN) algorithm [63, 64] was used for searching the TS geometries [65, 66], which were confirmed through vibrational frequency computations. Then, reactions leading toward the $[5, 6]$ and $[6, 6]$ reaction pathways were followed through the intrinsic reaction coordinate (ξ, IRC) by means of the IRC procedure as implemented in *Gaussian09* [37–39, 67]. The cutoffs used to ensure the C_s point group in the IRC computations were set to be loose (threshold of 0.1 Å). Single point calculations on the gas-phase M06-2X geometries were computed using the domain-based local pair-natural orbital coupled cluster (DLPNO-CCSD(T)) scheme [68–72] in conjunction with the cc-pVTZ basis set [73]. An auxiliary cc-pVTZ basis set for Coulomb integrals was also included in the calculations [74]. The Orca 4.0.1 Software package was used for the DLPNO-CCSD(T)/cc-pVTZ computations [75].

For comparative purposes the profiles are presented in a reduced reaction coordinate (RRC, ξ_i^*) in which reactants and products at ξ_R^* and ξ_P^* are 0 and 1, respectively. Each point on the RRC (ξ_i^*) is computed as follows

$$\xi_i^* = \frac{\xi_i - \xi_R}{\xi_P - \xi_R} \tag{10}$$

were ξ_i corresponds to the IRC. It is worth mentioning that the RRC is used only for comparative purposes and does not carry any physical meaning. The are two ways to get numerical derivatives using RRC. First, numerical derivatives can be evaluated using the native reaction coordinate obtained through the IRC computation (ξ) and then plotting the derivative value against the RRC ξ^* obtained in Eq. (10). The second method is by multiplying the derivative of a given property $A(\xi)$ obtained in RRC by a correction factor Ω_n as,

$$A(\xi) = \Omega_n \frac{d^n}{d\xi^{*n}} A(\xi^*), \qquad \Omega_n = \frac{1}{(\xi_P - \xi_R)^n} \tag{11}$$

4   Results and Discussions

The cycloaddition reaction between C_{60} and cyclopentadiene was computed along the reaction coordinate, energy profiles for the $[5,6]$ and $[6,6]$ pathways are displayed in Figure 3(a). Activation energies in toluene solution with zero-point corrections computed at the M06-2X/6-31G(d) level were found to be 24.02 and 16.91 kcal mol⁻¹ for the $[5,6]$ and $[6,6]$ reaction pathways, while the predicted reaction energies are 5.4 and -19.11 kcal mol⁻¹ (both activation and reaction energies reported above were computed using the energy of the isolated reactants). [1] As previously reported [29, 76], the occurrence of the $[6,6]$ cycloaddition is favored both kinetically and thermodynamically due to its relatively small activation energy and more exoenergetic character compared to that of the $[5,6]$ reaction. By inspection of the energy profiles shown in Figure 3(a) it can be seen that both reaction pathways can be classified as an anti-Hammond reaction with a late transition state closer to the product ($\xi^* > 0.5$) [77].

Experimentally, it has been found that the reaction product of the $[4+2]$ cycloaddition reaction between C_{60} and cyclopentadiene only gives the $[6,6]$ adduct, without manifestation of subsequent ring openings [28, 78, 79]. Reactions of C_{60} with cyclopentadiene and other dienophiles have been experimentally reported, in which the cycloadducts formed are sometimes unstable and prone to undergo the formation of the initial reactants with elevation of temperature [26, 80, 81]. The available experimental data shows that the activation energy for the cycloaddition between C_{60} and cyclopentadiene is 6.9 kcal mol⁻¹ as reported by Pang and Wilson [80]. Furthermore, Giovanne et al. reported an activation energy of 26.7±2.2 kcal mol⁻¹ for the corresponding retro Diels Alder reaction [81]. From the suitable substraction of these two numbers, the experimental reaction energy can be estimated to be -19.8±2.2 kcal mol⁻¹ [76]. The activation enthalpy of reaction in terms of the reactant complex and the isolated reactants, $\Delta H^{\ddagger}$ and $\Delta H^{\ddagger}_{isol}$, for the $[6,6]$ path in toluene solution were 18.7 and 23.9 kcal mol⁻¹, respectively. Furthermore, the corresponding reaction enthalpy energies, ΔH° and ΔH°_{isol}, were found to be -22.3 and -19.9 kcal mol⁻¹. Clearly the obtained activation energies disagree with the activation barriers experimentally obtained. When the M06-2X/6-31G(d)

---

[1]These values are slightly different from those coming out from the energy profiles of Figure 3 where no ZPE correction is included.

method is used as a part of the two-layered ONIOM approach (ONIOM2), ONIOM2(M06-2X/6-31G(d):SVWN/STO-3G), an activation energy of 8.2 kcal mol^{-1} is obtained referenced to the reactant complex and 12.1 kcal mol^{-1} relative to the isolated reactants, the latter very close to the experimental value [76]. For a more detailed discussion of the activation energies with respect to the level of theory, the reader is referred to ref [76].

To gain insights into the reaction mechanism the RF was obtained, and it is displayed in Figure 3(b). Within the RF formalism, the reaction coordinate can be divided into regions where different reaction mechanisms might be operating. The limits of the reaction regions are denoted by vertical dashed lines in black and red for the $[5, 6]$ and $[6, 6]$ reaction channels, respectively. For numerical results extracted from the RF formalism, refer to Table 1. On one hand, it is worth noting that when the two pathways are compared, the same percentage of structural and electronic expending is exhibited: 73% of the energy barrier is mainly used in structural reorganizations to reach the TS structure, whereas only a 27% of $\Delta E^{\ddagger}$ accounts of electronic expenditure. This result is consistent with the work of Fernández *et. al.*, where the deformation energy obtained by the activation-strain model was quite similar for the [5,6] and [6,6] attack [29]. On the other hand, solely in terms of energy, clearly the $[5, 6]$ pathway exhibits both structural and electronic energies larger than the $[6, 6]$ pathway, which explains the higher activation energy obtained for the $[5, 6]$ path.

| **Reaction**	$\Delta E^{\ddagger}$	ΔE°	$W_1(\%\Delta E^{\ddagger})$	$W_2(\%\Delta E^{\ddagger})$
$[5, 6]$ pathway	26.84	-0.75	19.63 (73)	7.21 (27)
$[6, 6]$ pathway	11.22	-22.38	8.18 (73)	3.04 (27)

Table 1: Activation and reaction energies extracted from energy profiles obtained through the IRC procedure in gas phase at the M06-2X/6-31G(d) level of theory. The reaction works (W_i) computed from the reaction force analysis are also quoted. Energetic values reported in kcal mol^{-1}.
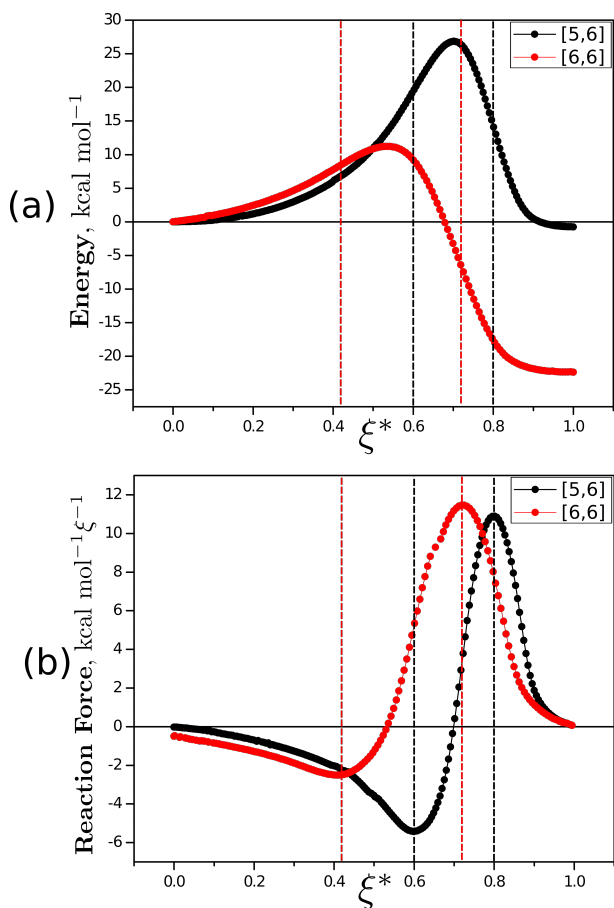
Figure 3: Energy (a) and reaction force profiles (b) for the cycloaddition between C_{60} and cyclopentadiene computed in gas phase. The [5,6] and [6,6] reaction is represented in black and red, respectively. Energies computed at the M06-2X/6-31G(d) level of theory. Vertical dashed lines correspond to the minimum and maximum of the reaction force. These vertical lines divide the reaction coordinate into reactant, transition state and product regions, respectively. In the reduced reaction coordinate, $\xi^* = 0$ is the reactant complex and $\xi^* = 1$ is the product complex (both with C_s symmetry).

To obtain more reliability regarding activation and reaction energies and to validate the level of theory used in this study, we have computed coupled cluster energies with single, double and perturbative triple excitations (CCSD(T)) using the DLPNO scheme as implemented in the *Orca* software. Coupled cluster energies were computed over the M06-2X geometries previously optimized, and it was verified that they correspond to a minimum or a transition state (see Computational Details Section). In Figure 4, energies for both reaction pathways are

presented. As can be seen from Figure 4, the formation of the reactant complex is exoenergetic and interestingly both reactant complexes lie roughly at the same energy. The latter result indicates that the energetic difference between both reaction paths arises after formation of the reactant complex, and therefore formation of the reactant complex does not play a significant role in the obtention of the activation barriers. In this regard, activation energies were found to be 26.4 and 11.6 kcal mol^{-1}, while reaction energies amount to -2.7 and -22.2 kcal mol^{-1} for the $[5, 6]$ and $[6, 6]$ paths. Interestingly, the DLPNO-CCSD(T) energies agrees exceptionally well with those obtained using the M06-2X functional. This not only confirms the good choice of the methodology but also the reliability of the results here presented.
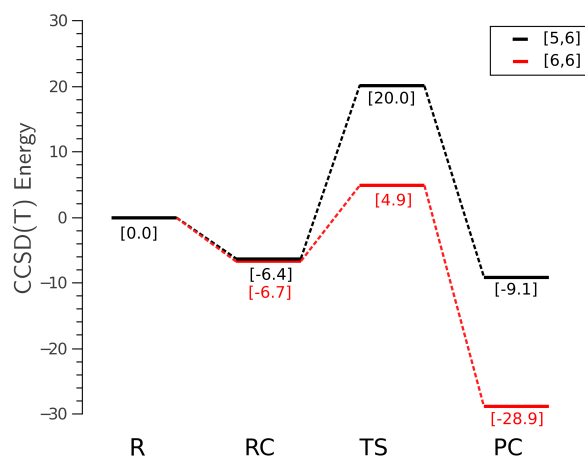
Figure 4: DPLNO-CCSD(T)/cc-pVTZ energies for the $[5, 6]$ and $[6, 6]$ paths for the cycloaddition between C_{60} and cyclopentadiene. Energetics are in kcal mol^{-1}.

14

4.1 Symmetry-Adapted Reaction Electronic Flux

In this section the SA-REF profiles are discussed. The C_s symmetry pathway in which the cycloaddition between C_{60} and cyclopentadiene takes place allows the obtention of two SA-REFs: $J_{A'}(\xi^*)$ and $J_{A''}(\xi^*)$, following the irreducible representation of $\mathcal{G}$. The $J_{A'}(\xi^*)$ and $J_{A''}(\xi^*)$ fluxes account for π and σ bonding information as previously reported [62]. The symmetrized orbital representation (A' and A'') along with the wavefunction of the reaction under consideration is depicted in Figure 5. The $J_{A'}(\xi^*)$ is obtained from the symmetric $109a'$ and $110a'$ orbitals whereas $J_{A''}(\xi^*)$ is computed from the antisymmetric $89a''$ and $90a''$ orbitals. The total REF is then obtained as $J(\xi) = J_{A'}(\xi^*) + J_{A''}(\xi^*)$. It is worth noting that the $90a''$ molecular orbital for the $[5,6]$ pathway correspond to the LUMO+1 while for the $[6,6]$ pathway the LUMO+2 is used (molecular orbital isosurfaces can be seen in Supporting Information).
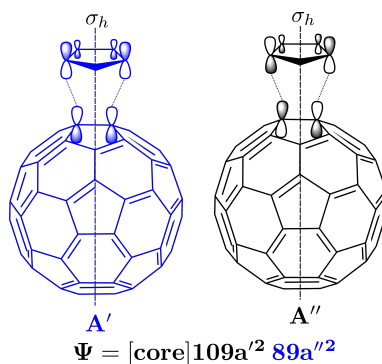
Figure 5: A' and A'' orbital interactions for cycloaddition between fullerene and C_{60}. Only representative p orbitals are represented in C_{60}. The dotted line represents the σ_h molecular plane. The system's wave function is shown below the orbital representation.

In the present cycloaddition mechanisms (for both $[5,6]$ and $[6,6]$ paths), three π bonds are broken: one in C_{60} (C1-C1') and two in cyclopentadiene (C_α-C_β and $C_{\alpha'}$-$C_{\beta'}$). Moreover, one π (C_β-$C_{\beta'}$) and two σ bonds (C1-C_α and C1'-$C_{\alpha'}$) are formed.

The total electronic activity and what accounts for π and σ reordering in the $[5,6]$ and $[6,6]$ reaction pathways are shown in Figures 6 and 7, respectively. Starting with the $[5,6]$ path, it can be seen in the $J(\xi^*)$ profile that a non-spontaneous electronic activity starts to drive the reaction from the very beginning until reaching a minimum at the end of the **RR** (force minimum). Therefore, in the **RR**, bond weakening/breaking dominates in this stage of the mechanism. At the REF minimum, the electron flux experiences a step; it increases sharply up to reach a maximum at the end of the **TSR**. This change is reflected by means of an increment of the electronic activity, a fingerprint that bond forming processes are predominant at this stage of the mechanism. Then, the total REF decreases until reaching the product complex structure with $J(\xi^*) = 0$. When the $J(\xi^*)$ are compared between the $[5,6]$ and the $[6,6]$ mechanism in Figures 6 and 7, respectively, it can be observed that the same electronic pattern is found for both reactions: both the REF's minimum and maximum coincide with RF's minimum and maximum. However, the electron flux is more intensive in the $[5,6]$ path than the observed in the $[6,6]$ one. This fact has a preponderant influence on the difference observed in the activation energies: the more extensive electronic reordering in the activation process, the larger activation energy is found. This general pattern has been reported previously [82].

To gain more information in the electronic activity that takes place along the reaction, the $J_{A'}(\xi^*)$ and $J_{A''}(\xi^*)$ fluxes are discussed hereafter. In general, it is observed that $J_{A''}(\xi^*)$ prevails over the $J_{A'}(\xi^*)$ for both cycloadditions along the entire reaction coordinate, although these differences are stressed at the flux minimum.

Regarding the $J_{A'}(\xi^*)$ profile for the $[5,6]$ path, it is negative all along the **RR**. The main event here is the weakening of the π bonds centered in the C1-C1' bond in fullerene and the C_α-C_β and $C_{\alpha'}$-$C_{\beta'}$ bonds in cyclopentadiene (see Figure 1 for labeling of atoms). The weakening

and subsequent breaking of these bonds is prompted by an strong Pauli electrostatic repulsion as the reactants approach one another [44, 62]. At the $J_{A'}(\xi^*)$ minimum denoted by **(I)**, it is observed that the C_α-C_β and $C_{\alpha'}$-$C_{\beta'}$ bonds have only changed by 0.01 Å. The C1-C1′ bond remains unchanged with respect to the **(RC)** structure, which supports the idea that up to this point weakening over breaking processes are taking place. Subsequent to **(I)** the π electronic activity, captured by $J_{A'}(\xi^*)$, is driven toward positive values passing through the **(TS)** structure and reaching a maximum at **(III)**. It is worth noting that at the TS structure the C_α-C_β and C_β-$C_{\beta'}$ bond distances are very close with values of 1.41 and 1.39 Å, respectively, denoting a highly delocalized cyclopentadiene moiety. At **(III)**, the formation of the πC_β-$C_{\beta'}$ bond is carried out, according to the $J_{A'}(\xi^*)$ pattern. Afterwards, the π electronic activity decreases toward zero, where the π bonds both in fullerene and cyclopentadiene are formed.

The $J_{A''}(\xi^*)$ profile in Figure 6 shows the electronic reordering for σ electrons according with the SA-REF scheme. In the $J_{A''}(\xi^*)$ profile the electronic activity also decreases from the onset of the reaction until reaching a minimum at **(II)** located within the **TSR**. This non-spontaneous electronic activity is observed due to the weakening of the σ bonds neighboring the C1 and C1′ carbon atoms in fullerene, as a consequence of the pyramidalisation of this above-mentioned atoms in the transition $sp^2 \longrightarrow sp^3$. This negative peak has not been observed before for similar DA reactions [62]. When the electronic activity reaches a minimum, it increases sharply until it encounter a maximum at **(IV)**. At this spontaneous reordering, the formation of the cycloadduct by means of the synchronous formation of the two σ bonds between C1-C_α and C1′-$C_{\alpha'}$ is evidenced. At the **(IV)** stage, the bond distance of the C1-C_α and C1'-$C_{\alpha'}$ is 1.79 Å, suggesting a loosely bonded complex. Afterwards the electronic activity decreases toward the equilibrium condition, reaching zero. At the **(PC)** structure the σ bonds formed at **(IV)** are strengthened and they acquire a distance of 1.58 Å. Moreover, it is worth mention that an adjacent bond to the C1-C1′ has been tracked along the reaction coordinate from **(RC)** to **(PC)**, and has been selected to account for the pyramidalization toward the formation of the new simple bonds. As may be seen, this bond changes in length from 1.45 to 1.53 Å. Similar distortions take place in the vicinal bonds to start the σ bond formation.

Regarding the $[6,6]$ fluxes, similar tendencies and results are extracted from $J(\xi^*)$, $J_{A'}(\xi^*)$ and $J_{A''}(\xi^*)$. The minimum and maximum of the REF and SA-REFs have the same interpretation as those observed for the $[5,6]$ reaction pathway. Furthermore, some differences along the two reaction paths will be discussed hereafter. Since some differences in terms of the total REF were discussed above, special attention will be devoted to the SA-REFs, with the aim of finding differences along the two competitive paths. When the $J_{A'}(\xi^*)$ is compared between both pathways (Figures 6 and 7) it can be seen that both minima lie at the same magnitude ca. -0.5 kcal mol$^{-1}\xi^{-1}$, whereas the maximum in these profiles differs slightly, being of larger magnitude for the $[5,6]$ pathway than that obtained for the $[6,6]$ one. As shown in ref. [29], this difference can be attributed to the lower orbital interactions along the reaction coordinate for the $[5,6]$ attack as compared to the $[6,6]$ path.
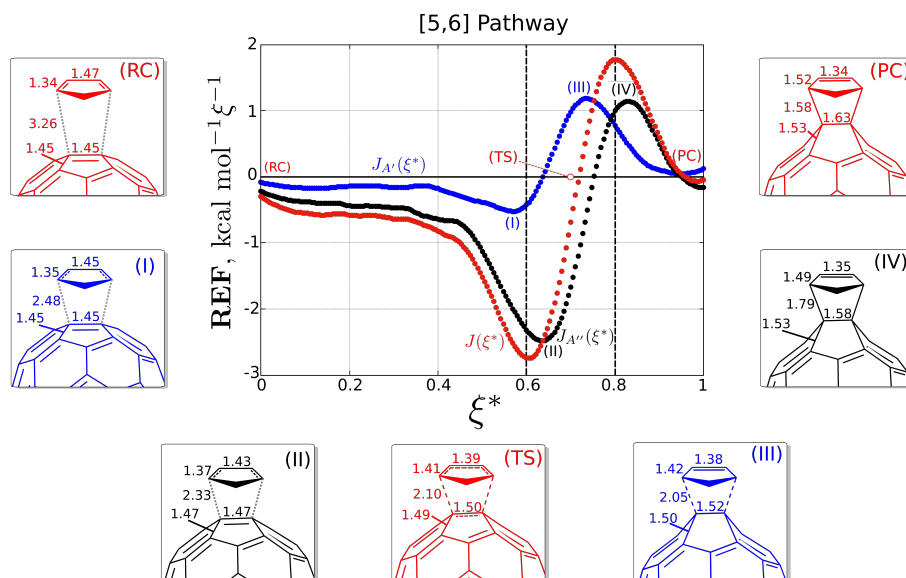
Figure 6: Total, A' and A'' electron fluxes represented by $J(\xi^*)$, $J_{A'}(\xi^*)$ and $J_{A''}(\xi^*)$, respectively, for the $[5,6]$ pathway. Structures at key points along the reaction coordinate are shown. Distances are given in Angstroms. Vertical dashed lines correspond to the minimum and maximum of the reaction force. They divide the reaction coordinate into reactant, transition state and product regions, respectively. In the reduced reaction coordinate, $\xi^* = 0$ is the reactant complex and $\xi^* = 1$ is the product complex (both with C_s symmetry).
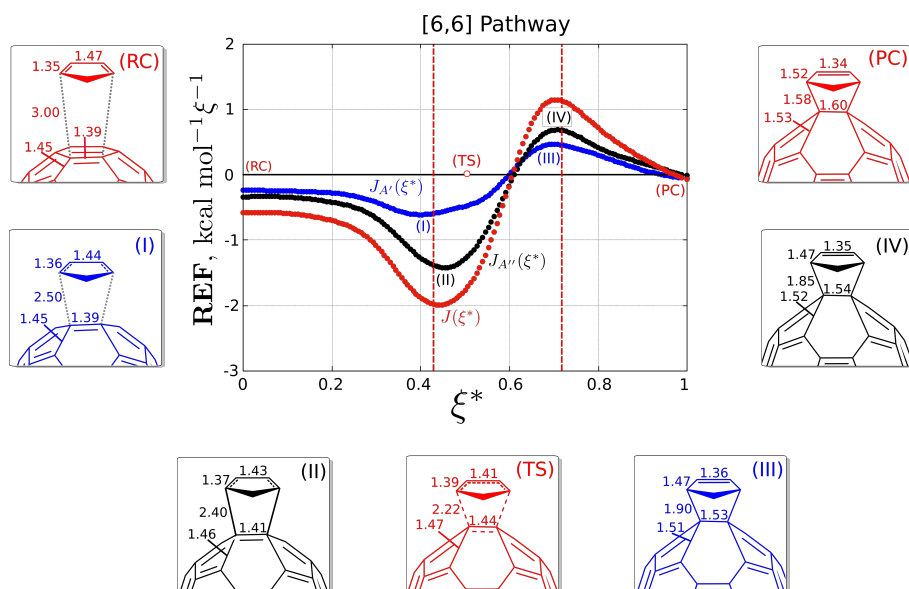
Figure 7: Total, A' and A'' electron fluxes represented by $J(\xi^*)$, $J_{A'}(\xi^*)$ and $J_{A''}(\xi^*)$, respectively, for the $[6,6]$ pathway. Structures at key points along the reaction coordinate are shown. Distances are given in Angstroms. Vertical dashed lines correspond to the minimum and maximum of the reaction force. They divide the reaction coordinate into reactant, transition state and product regions, respectively. In the reduced reaction coordinate, $\xi^* = 0$ is the reactant complex and $\xi^* = 1$ is the product complex (both with C_s symmetry).

4.2 Symmetry-Adapted Kinetic Energy

Kinetic energy of the electrons comes from the application of a one-electron Hermitian operator whose eigenvalues do not vary through a symmetry operation. On this basis, the obtention of kinetic energy values belonging to a different irreducible irrepresentations is possible given the molecular symmetry. In Figure 8, the kinetic energies associated with each irreducible representation of the C_S group are shown for each reaction path. $T_{A'}(\xi^*)$ and $T_{A''}(\xi^*)$ represent the kinetic energies of the electrons that occupy the orbitals that transform to the A' and A'' irreducible representations, respectively. In Figure 8(a), the $T_{A'}(\xi^*)$ for both reactions are shown. In this plot two maxima are obtained that account for the π electronic activity, and they are located at $\xi^* \approx 0.5$ and $\xi^* \approx 0.3$ (for the $[5,6]$ and $[6,6]$ reaction, respectively), which are almost at the same position of the respective $J_{A'}(\xi^*)$ values shown in Figures 6

and 7. At the same time, a minimum for both pathways is observed once leaving the **TSR** that lies almost at the same position where the maximum of the $J_{A'}(\xi^*)$ is observed in Figures 6 and 7. This decrease of the kinetic energy for both irreducible representations in the vicinity of the transition state structure suppose the increase in aromaticity of the transient species, since the TS structures of allowed pericyclic reactions are well known to be aromatic (cite). The variation of the kinetic energy along the path indicates that when a bond is being weakened or broken (negative REF values) an increase in the kinetic energy is observed, which promotes a contraction of the electronic density. Conversely, when a bond is being formed or strengthened, a decrease of the kinetic energy is observed, promoting an expansion of the electronic density. Such a pattern has been reported previously by Doubleday and Houk for a series of Diels-Alder reactions [83]. The authors obtained the mean kinetic energy obtained from molecular dynamics and plotted it against the forming C–C bond distances. It was found that in the transition zone a dip in the mean kinetic energy is observed. As the C–C bond stretching dominates the transition vector for Diels-Alder reactions, the kinetic energy is a good proxy for the "flux"[2] along the reaction coordinate. This is in agreement with our results in which the minima/maxima observed in the REF profile are in close agreement with the maxima/minima observed in the kinetic energy plots. The same conclusion can be drawn by inspection of the $T_{A''}(\xi^*)$ values with respect to the $J_{A''}(\xi^*)$ minima and maxima.

It is worth mention that in Figure 8(a) no noticeable differences in the two maxima or minima are observed. However, in Figure 8(b) a huge difference in the $T_{A''}(\xi^*)$ energy is observed at the maximum for both reaction pathways. The above mentioned maxima lies almost at the same position where weakening of the σ bonds is carried out, which is observed as a negative peak in the $J_{A''}(\xi^*)$ profiles in Figures 6 and 7. Interestingly, the difference in magnitude of the negative peak observed in the $J_{A''}(\xi^*)$ profile for both reaction pathways can be understood by the positive peaks observed in $T_{A''}(\xi^*)$. Thus, the larger σ electronic activity observed in the $[5, 6]$ path caused by the weakening of the σ bonds neighboring the C1 and C1$'$ carbon

---

[2]The "flux" reported by Doubleday and Houk differs from the definition of the REF. The "flux" is referred to the fingerprint of transition state theory, i.e., the TS is the minimum flux of forward-moving trajectories – the dynamical bottleneck.

atoms (prompted by the $sp^2 \longrightarrow sp^3$ transition) is fully consistent with a larger kinetic energy for those σ electrons.
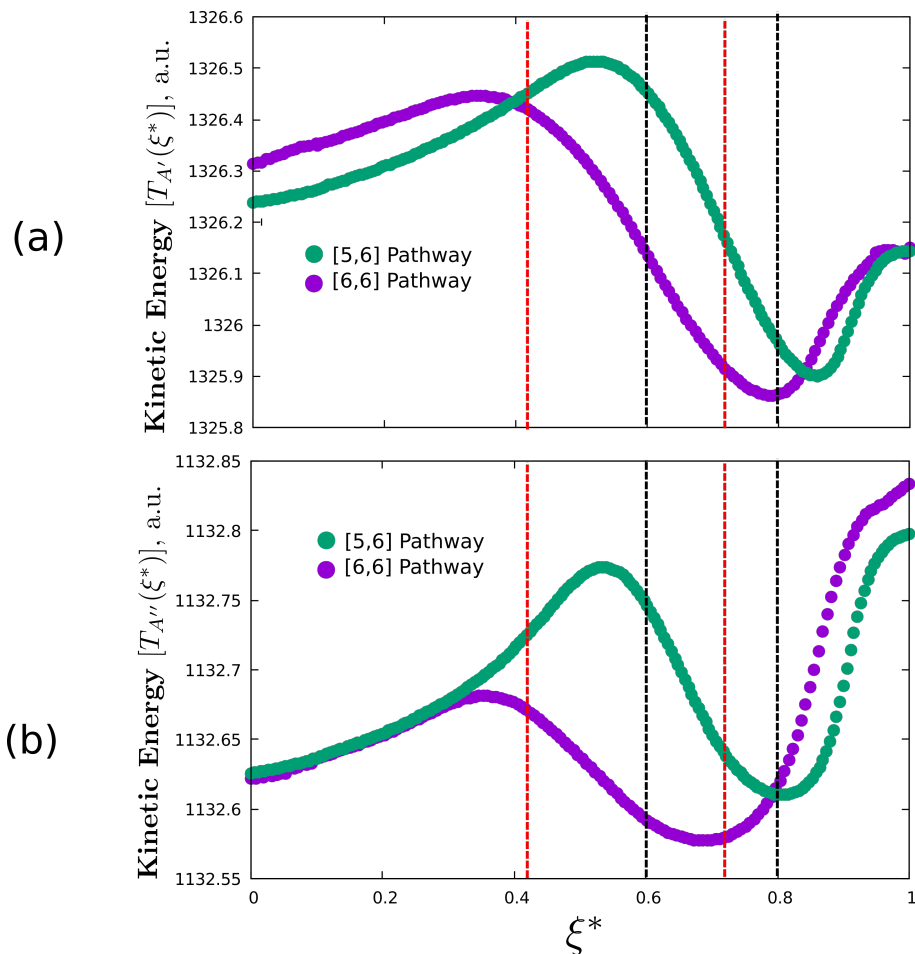
Figure 8: Kinetic energies computed for each irreducible representation $(T_{\Gamma_i}(\xi^*))$ along the reaction coordinate. (a) A' kinetic energy $[T_{A'}(\xi^*)]$ and (b) A'' kinetic energy $[T_{A''}(\xi^*)]$for the $[5,6]$ and $[6,6]$ reaction pathways. Vertical dashed lines correspond to the minimum and maximum of the reaction force, they are black and red for the $[5,6]$ and $[6,6]$ path, respectively. These vertical lines divide the reaction coordinate into reactant, transition state and product regions, respectively. In the reduced reaction coordinate, $\xi^* = 0$ is the reactant complex and $\xi^* = 1$ is the product complex (both with C_s symmetry).

5   Conclusions

We have analyzed the two reaction mechanisms of the cycloaddition reaction between C_{60} and cyclopentadiene corresponding to the $[5,6]$ and $[6,6]$ attacks. Partition of the total reaction electronic flux $J(\xi^*)$ into $J_{A'}(\xi^*)$ and $J_{A''}(\xi^*)$ contributions allowed us to understand whether π and/or σ bonding changes take place along the progress of the reaction. The $J_{A'}(\xi^*)$ facilitates understanding the π reordering, whereas $J_{A''}(\xi^*)$ accounts for σ bonding changes. It was found that the $[6,6]$ path prevails over the $[5,6]$ due to a lower activation energy and larger exothermicity. With the use of the SA-REF it was found that the dominating event that drives the appearance of the differences in activation energies between the $[5,6]$ and $[6,6]$ path is due to a non-spontaneous σ electronic activity, which appears as a result of the weakening of the C–C bonds due to pyramidalization of the C1, C1', C_{α} and $C_{\alpha'}$ carbon atoms. Inspection of the kinetic energy of both irreducible representations showed that when a bond is being weakened/broken (negative values of REF) an increase in the kinetic energy occurs which we associate with a contraction of the electronic density in the vicinity of the chemical event. Conversely, when a bond is being formed/strengthened (positive REF values) a decreasing of the kinetic energy is observed and therefore an expansion of the electronic density occurs. Moreover, the decrease of the kinetic energy of electrons suppose the increase in aromaticity in the vecinity of the transition state. The SA-REF is a useful tool derived from a global property that gives valuable information about local bonding changes taking place along a reaction pathway.

Graphical Abstract

References

[1] Guldi, D. M.; Martin, N. *Fullerenes: from synthesis to optoelectronic properties*; Springer Science & Business Media, 2013; Vol. 4.

[2] De La Puente, F. L.; Nierengarten, J.-F. *Fullerenes: principles and applications*; Royal Society of Chemistry, 2011.

[3] Martín, N. *Chem. Comm.* **2006**, 2093–2104.

[4] Martin, N.; Altable, M.; Filippone, S.; Martín-Domenech, A. *Synlett* **2007**, *2007*, 3077–3095.

[5] Hirsch, A. *Fullerenes and Related Structures*; Springer, 1999; pp 1–65.

[6] Hirsch, A.; Brettreich, M. *Fullerenes: chemistry and reactions*; John Wiley & Sons, 2006.

[7] Martín, N.; Altable, M.; Filippone, S.; Martín-Domenech, Á. *Chem. Comm.* **2004**, 1338–1339.

[8] Martín, N.; Altable, M.; Filippone, S.; Martín-Domenech, Á.; Poater, A.; Solà, M. *Chem. Eur. J.* **2005**, *11*, 2716–2729.

[9] Martínez, J. P.; Vizuete, M.; Arellano, L. M.; Poater, A.; Bickelhaupt, F. M.; Langa, F.; Solà, M. *Nanoscale* **2018**, *10*, 15078–15089.

[10] Mori, S.; Nambo, M.; Chi, L.-C.; Bouffard, J.; Itami, K. *Org. lett.* **2008**, *10*, 4609–4612.

[11] Nambo, M.; Noyori, R.; Itami, K. *J. Am. Chem. Soc.* **2007**, *129*, 8080–8081.

[12] Fagnou, K.; Lautens, M. *Chem. Rev.* **2003**, *103*, 169–196.

[13] Nambo, M.; Segawa, Y.; Wakamiya, A.; Itami, K. *Chem–Asian J.* **2011**, *6*, 590–598.

[14] Hsiao, T.-Y.; Santhosh, K.; Liou, K.-F.; Cheng, C.-H. *J. Am. Chem. Soc.* **1998**, *120*, 12232–12236.

[15] Inoue, H.; Yamaguchi, H.; Suzuki, T.; Akasaka, T.; Murata, S. *Synlett* **2000**, *2000*, 1178–1180.

[16] Artigas, A.; Pla-Quintana, A.; Lledó, A.; Roglans, A.; Solà, M. *Chem. Eur. J.* **2018**, *24*, 10653–10661.

[17] Śliwa, W. *Fullerenes, Nanotubes, and Carbon Nanostructures* **1997**, *5*, 1133–1175.

[18] Maynollo, J.; Kräutler, B. *Fullerene Science & Technology* **1996**, *4*, 213–226.

[19] Kräutler, B.; Maynollo, J. *Tetrahedron* **1996**, *52*, 5033–5042.

[20] others,, et al. *Carbon* **2018**, *129*, 286–292.

[21] Ueno, H.; Kawakami, H.; Nakagawa, K.; Okada, H.; Ikuma, N.; Aoyagi, S.; Kokubo, K.; Matsuo, Y.; Oshima, T. *J. Am. Chem. Soc.* **2014**, *136*, 11162–11167.

[22] Yao, J.; Xiao, Z.; Zhang, J.; Yang, X.; Gan, L.; Zhang, W.-X. *Chem. Comm.* **2008**,

[23] Wudl, F. *Acc. Chem. Res.* **1992**, *25*, 157–161.

[24] Kräutler, B.; Müller, T.; Maynollo, J.; Gruber, K.; Kratky, C.; Ochsenbein, P.; Schwarzenbach, D.; Bürgi, H.-B. *Angew. Chem. Int. Ed.* **1996**, *35*, 1204–1206.

[25] Hirsch, A.; Lamparth, I.; Grösser, T.; Karfunkel, H. R. *J. Am. Chem. Soc.* **1994**, *116*, 9385–9386.

[26] Wang, G.-W.; Saunders, M.; Cross, R. J. *J. Am. Chem. Soc.* **2001**, *123*, 256–259.

[27] Kroto, H. *Nature* **1987**, *329*, 529.

[28] Solá, M.; Mestres, J.; Martí, J.; Duran, M. *Chem. Phys. Lett.* **1994**, *231*, 325–330.

[29] Fernández, I.; Solà, M.; Bickelhaupt, F. M. *Chem. Eur. J.* **2013**, *19*, 7416–7422.

[30] Osuna, S.; Valencia, R.; Rodríguez-Fortea, A.; Swart, M.; Solà, M.; Poblet, J. M. *Chem. Eur. J.* **2012**, *18*, 8944–8956.

[31] Garcia-Borràs, M.; Osuna, S.; Swart, M.; Luis, J. M.; Solà, M. *Chem. Comm.* **2013**, *49*, 1220–1222.

[32] El Bakouri, O.; Garcia-Borràs, M.; Girón, R. M.; Filippone, S.; Martín, N.; Solà, M. *Phys. Chem. Chem. Phys.* **2018**, *20*, 11577–11585.

[33] Garcia-Borràs, M.; Osuna, S.; Luis, J. M.; Swart, M.; Solà, M. *Chem. Soc. Rev.* **2014**, *43*, 5089–5105.

[34] Popov, A. A.; Yang, S.; Dunsch, L. *Chem. Rev.* **2013**, *113*, 5989–6113.

[35] Toro-Labbé, A. *J. Phys. Chem. A* **1999**, *103*, 4398–4403.

[36] Toro-Labbé, A.; Gutiérrez-Oliva, S.; Murray, J.; Politzer, P. *Mol. Phys.* **2007**, *105*, 2619–2625.

[37] Fukui, K. *Acc. Chem. Res.* **1981**, *14*, 363–368.

[38] Hratchian, H. P.; Schlegel, H. B. *J. Chem. Phys.* **2004**, *120*, 9918–9924.

[39] Hratchian, H. P.; Schlegel, H. B. *J. Chem. Theory and Comp.* **2005**, *1*, 61–69.

[40] Martínez, J.; Toro-Labbé, A. *Chem. Phys. Lett.* **2004**, *392*, 132–139.

[41] Gutiérrez-Oliva, S.; Herrera, B.; Toro-Labbé, A.; Chermette, H. *J. Phys. Chem. A* **2005**, *109*, 1748–1751.

[42] Duarte, F.; Toro-Labbé, A. *J. Phys. Chem. A* **2011**, *115*, 3050–3059.

[43] Politzer, P.; Toro-Labbé, A.; Gutiérrez-Oliva, S.; Herrera, B.; Jaque, P.; Concha, M. C.; Murray, J. S. *J. Chem. Sci.* **2005**, *117*, 467–472.

[44] Politzer, P.; Murray, J. S.; Yepes, D.; Jaque, P. *J. Mol. Model.* **2014**, *20*, 1–6.

[45] Ortega, D. E.; Gutiérrez-Oliva, S.; Tantillo, D. J.; Toro-Labbé, A. *Phys. Chem. Chem. Phys.* **2015**, *17*, 9771–9779.

[46] Polanyi, J. C.; Zewail, A. H. *Acc. Chem. Res.* **1995**, *28*, 119–132.

[47] Zewail, A. H. *J. Phys. Chem. A* **2000**, *104*, 5660–5694.

[48] Villegas-Escobar, N.; Gutiérrez-Oliva, S.; Toro-Labbé, A. *J. Phys. Chem. C* **2015**, *119*, 26598–26604.

[49] Rincón, E.; Jaque, P.; Toro-Labbé, A. *J. Phys. Chem. A* **2006**, *110*, 9478–9485.

[50] Herrera, B.; Toro-Labbé, A. *J. Phys. Chem. A* **2007**, *111*, 5921–5926.

[51] Echegaray, E.; Toro-Labbé, A. *J. Phys. Chem. A* **2008**, *112*, 11801–11807.

[52] Parr, R.; Yang, W. *Density-Functional Theory of Atoms and Molecules*; Oxford University Press: New York, 1989.

[53] Pearson, R. G. *J. Am. Chem. Soc.* **1985**, *107*, 6801–6806.

[54] Chermette, H. *J. Comp. Chem.* **1999**, *20*, 129–154.

[55] Geerlings, P.; De Proft, F.; Langenaeker, W. *Chem. Rev.* **2003**, *103*, 1793–1874.

[56] Janak, J. *Phys. Rev. B* **1978**, *18*, 7165.

[57] Vogt-Geisse, S.; Toro-Labbé, A. *J. Chem. Phys.* **2009**, *130*, 244308.

[58] Giri, S.; Echegaray, E.; Ayers, P. W.; Nuñez, A. S.; Lund, F.; Toro-Labbé, A. *J. Phys. Chem. A* **2012**, *116*, 10015–10026.

[59] Inostroza-Rivera, R.; Herrera, B.; Toro-Labbé, A. *Phys. Chem. Chem. Phys.* **2014**, *16*, 14489–14495.

[60] Morell, C.; Tognetti, V.; Bignon, E.; Dumont, E.; Hernández-Haro, N.; Herrera, B.; Grand, A.; Gutiérrez-Oliva, S.; Joubert, L.; Toro-Labbé, A.; Chermette, H. *Theor. Chem. Acc.* **2015**, *134*, 133.

[61] Vogt-Geisse, S.; Toro-Labbé, A. *J. Comput. Chem.* **2016**, *37*, 1794–1800.

[62] Villegas-Escobar, N.; Vogt-Geisse, S.; Gutiérrez-Oliva, S.; Toro-Labbé, A. *Theor. Chem. Acc.* **2016**, *135*, 1–8.

[63] Peng, C.; Bernhard Schlegel, H. *Israel J. Chem.* **1993**, *33*, 449–454.

[64] Peng, C.; Ayala, P. Y.; Schlegel, H. B.; Frisch, M. J. *J. Comp. Chem.* **1996**, *17*, 49–56.

[65] Schlegel, H. B. *J. Comp. Chem.* **1982**, *3*, 214–218.

[66] Schlegel, H. B. *Adv. Chem. Phys.* **2009**, 249.

[67] Frisch, M. J. et al. Gaussian Inc. Wallingford CT 2009.

[68] Riplinger, C.; Neese, F. *J. Chem. Phys.* **2013**, *138*, 034106.

[69] Riplinger, C.; Sandhoefer, B.; Hansen, A.; Neese, F. *J. Chem. Phys.* **2013**, *139*, 134101.

[70] Liakos, D. G.; Sparta, M.; Kesharwani, M. K.; Martin, J. M.; Neese, F. *J. Chem. Theory and Comput.* **2015**, *11*, 1525–1539.

[71] Liakos, D. G.; Neese, F. *J. Chem. Theory and Comput.* **2015**, *11*, 4054–4063.

[72] Paulechka, E.; Kazakov, A. *J. Phys. Chem. A* **2017**, *121*, 4379–4387.

[73] Dunning Jr, T. H. *J. Chem. Phys.* **1989**, *90*, 1007–1023.

[74] Weigend, F.; Köhn, A.; Hättig, C. *J. Chem. Phys.* **2002**, *116*, 3175–3183.

[75] Neese, F. *Wiley Interdiscip, Rev.: Comput. Mol. Sci.* **2012**, *2*, 73–78.

[76] Osuna, S.; Swart, M.; Solà, M. *J. Phys. Chem. A* **2011**, *115*, 3491–3496.

[77] Hammond, G. S. *J. Am. Chem. Soc.* **1955**, *77*, 334–338.

[78] Rotello, V. M.; Howard, J. B.; Yadav, T.; Conn, M. M.; Viani, E.; Giovane, L. M.; Lafleur, A. L. *Tetrahedron lett.* **1993**, *34*, 1561–1562.

[79] Solà, M.; Duran, M.; Mestres, J. *J. Am. Chem. Soc.* **1996**, *118*, 8920–8924.

[80] Pang, L. S.; Wilson, M. A. *J. Phys. Chem.* **1993**, *97*, 6761–6763.

[81] Giovane, L. M.; Barco, J. W.; Yadav, T.; Lafleur, A. L.; Marr, J. A.; Howard, J. B.; Rotello, V. M. *J. Phys. Chem.* **1993**, *97*, 8560–8561.

[82] Villegas-Escobar, N.; Vilhelmsen, M. H.; Gutiérrez-Oliva, S.; Hashmi, A. S. K.; Toro-Labbé, A. *Chem. Eur. J.* **2017**, 13360–13368.

[83] Black, K.; Liu, P.; Xu, L.; Doubleday, C.; Houk, K. N. *PNAS* **2012**, *109*, 12860–12865.